GEOPHYSICS, VOL. 56, NO. 12 (DECEMBER 1991); P. 2080–2089, 12 FIGS.

Elastic wave propagation using cylindrical coordinates

David Kessler* and Dan Kosloff‡

ABSTRACT

A pseudo-spectral method for a solution of the equations of dynamic elasticity in cylindrical coordinates is based on the Chebychev expansion in the radial direction and the Fourier expansion in the angular direction and is suitable for simulating wave propagation in the vicinity of cylindrical objects. The numerical grid consists of a series of concentric rings, each one with a separate Chebychev-Fourier mesh. One numerical grid is defined for the cylindrical cavity and another grid for the medium around the cavity. Combining these two numerical grids allows reduction of the number of grid points in the angular direction in the interior grid and thus increases the time step. This makes the use of polar coordinates much more economic.

The numerical algorithm is applicable to any arbitrary heterogeneous medium.

INTRODUCTION

The problem addressed in this work is two-dimensional elastic wave propagation in the vicinity of cylindrical objects. The motivation for such a study is to simulate phenomena associated with boreholes. A two dimensional study, in which the cylindrical geometry is tackled, is a first step towards constructing a full 3-D simulator for borehole measurement techniques such as vertical seismic profiling.

The algorithm described here is based on a direct solution in polar coordinates of the equations of momentum conservation and the stress strain relations for an isotropic solid. Solving in polar coordinates appears necessary because of the cylindrical geometry, since representing the cylindrical cavity using Cartesian coordinates would require a prohibitively fine spatial grid.

The numerical algorithm presented is based on a Chebychev expansion of the solution in the radial direction and a Fourier expansion for the angular direction (Figure 1). Integration of the equations in time is performed by a fourth order Runge-Kutta technique.

The numerical algorithm allows for complete material variability including fluids and solids in juxtaposition.

The same type of expansion has been used previously by Kessler and Kosloff (1990) for acoustic waves. The radial Chebychev expansion allows incorporation of boundary conditions which in the present case are an absorbing boundary condition at the outer radius of the grid ($r = b$), and a free-surface boundary condition on the cavity ($r = a$). In certain applications, a rigid boundary condition as well has been used for the cylindrical object.

For the enforcement of the boundary conditions, we used a stabilization procedure based on characteristic variables as described by Gottlieb et al. (1982), and Baylis et al. (1986). Unlike previous work with the Chebychev method (Kosloff et al., 1990; Kessler and Kosloff, 1990), the solution used for the one-dimensional diagonalized system of equations is only approximate, and we have found that the stabilization procedure works only when the ratio between the interior radius of the grid and the exterior radius is not too great. We thus adopted a multidomain approach in which the numerical grid consists of a series of concentric rings, each one with a separate Chebychev mesh (Tessmer et al., 1992). The continuity of the solution between the rings is enforced by using characteristic variables. Unlike with cylindrical grids in general, this approach allows a relatively uniform spatial sampling when needed or to change grid spacing in different regions.

The next section contains the equations of dynamic elasticity and the solution technique. The following one describes characteristic variables for the enforcement of boundary conditions and the multidomain approach. Finally, numerical examples test the algorithm against problems with known analytical solutions and demonstrate physical effects associated with the presence of the cylindrical cavity.

EQUATIONS OF MOTION AND SOLUTION SCHEME

The numerical algorithm is based on a solution of the equations of conservation of momentum combined with the

Presented at the 60th Annual International Meeting, Society of Exploration Geophysicists. Manuscript received by the Editor December 4, 1990; revised manuscript received June 6, 1991.
*Department of Geophysics, Tel Aviv University, Tel Aviv 69978, Israel.
‡Geophysical Development Corporation, 8401 Westheimer, Suite #150, Houston, Texas 77063.

stress-strain relation for an isotropic elastic solid undergoing infinitesimal deformation. For two dimensional cylindrical coordinates (r, θ) the equations of momentum conservation are (Fung, 1965):

$$\rho \ddot{U}_r = \frac{1}{r}\frac{\partial}{\partial r}(r\sigma_{rr}) + \frac{1}{r}\frac{\partial \sigma_{r\theta}}{\partial \theta} - \frac{\sigma_{\theta\theta}}{r} + f_r$$

and

$$\rho \ddot{U}_\theta = \frac{1}{r^2}\frac{\partial}{\partial r}(r^2\sigma_{r\theta}) + \frac{1}{r}\frac{\partial \sigma_{\theta\theta}}{\partial \theta} + f_\theta, \tag{1}$$

where U_r and U_θ are the displacements in r and θ directions; σ_{rr}, $\sigma_{\theta\theta}$, and $\sigma_{r\theta}$ are the stress components; f_r and f_θ are body forces per unit volume, and ρ is density. The stress-strain relations for an isotropic elastic solid expressed in terms of displacement derivatives in cylindrical coordinate are:

$$\sigma_{rr} = (\lambda + 2\mu)\frac{\partial U_r}{\partial r} + \frac{\lambda}{r}\frac{\partial U_\theta}{\partial \theta} + \frac{\lambda}{r}U_r,$$

$$\sigma_{\theta\theta} = \lambda\frac{\partial U_r}{\partial r} + \left(\frac{\lambda + 2\mu}{r}\right)\frac{\partial U_\theta}{\partial \theta} + \left(\frac{\lambda + 2\mu}{r}\right)U_r,$$

$$\sigma_{r\theta} = \frac{\mu}{r}\frac{\partial U_r}{\partial \theta} + \mu\frac{\partial U_\theta}{\partial r} - \frac{\mu}{r}U_\theta, \tag{2}$$

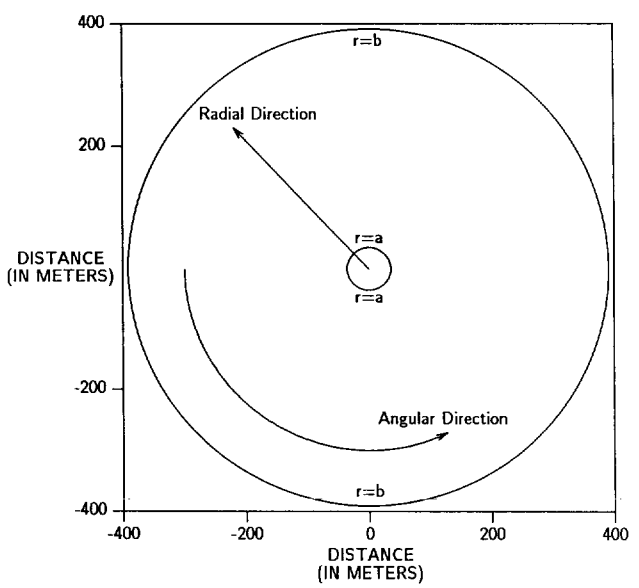

FIG. 1. Configuration of the problem, $r = a$ marks the cavity and $r = b$ marks the edges of the grid; a can be very small.

where λ and μ are respectively the rigidity and the shear modulus.

The treatment of the boundary conditions requires concurrent values of the variables $\dot{U}_r$, $\dot{U}_\theta$, σ_{rr}, $\sigma_{\theta\theta}$, and $\sigma_{r\theta}$. Thus we recast equations (1) and (2) as a system of five coupled first order equations given by:

$$\frac{\partial}{\partial t}\begin{bmatrix}\dot{U}_r\\ \dot{U}_\theta\\ \sigma_{rr}\\ \sigma_{\theta\theta}\\ \sigma_{r\theta}\end{bmatrix} = \underline{\mathbf{A}}\begin{bmatrix}\dot{U}_r\\ \dot{U}_\theta\\ \sigma_{rr}\\ \sigma_{\theta\theta}\\ \sigma_{r\theta}\end{bmatrix}_r + \underline{\mathbf{B}}\begin{bmatrix}\dot{U}_r\\ \dot{U}_\theta\\ \sigma_{rr}\\ \sigma_{\theta\theta}\\ \sigma_{r\theta}\end{bmatrix}_\theta + \begin{bmatrix}\frac{1}{\rho r}(\sigma_{rr} - \sigma_{\theta\theta})\\ \frac{2}{\rho r}\sigma_{r\theta}\\ \frac{\lambda}{r}\dot{U}_r\\ \frac{\lambda + 2\mu}{r}\dot{U}_r\\ -\frac{\mu}{r}\dot{U}_\theta\end{bmatrix} + \begin{bmatrix}\frac{f_r}{\rho}\\ \frac{f_\theta}{\rho}\\ 0\\ 0\\ 0\end{bmatrix}, \tag{3}$$

where

$$\underline{\mathbf{A}} = \begin{bmatrix} 0 & 0 & \frac{1}{\rho} & 0 & 0\\ 0 & 0 & 0 & 0 & \frac{1}{\rho}\\ \lambda + 2\mu & 0 & 0 & 0 & 0\\ \lambda & 0 & 0 & 0 & 0\\ 0 & \mu & 0 & 0 & 0\end{bmatrix} \quad \text{and}$$

$$\underline{\mathbf{B}} = \begin{bmatrix} 0 & 0 & 0 & 0 & \frac{1}{\rho r}\\ 0 & 0 & 0 & \frac{1}{\rho r} & 0\\ 0 & \frac{\lambda}{r} & 0 & 0 & 0\\ 0 & \frac{\lambda + 2\mu}{r} & 0 & 0 & 0\\ \frac{\mu}{r} & 0 & 0 & 0 & 0\end{bmatrix}. \tag{4}$$

The numerical algorithm solves equation (3) with appropriate boundary conditions at $r = a$ and at the edges of the numerical grid, at $r = b$ (Figure 1). The variables are

discretized on a spatial grid which is nonuniform in the r direction and uniform in the θ variable (Figure 2). Equation (3) contains both spatial and temporal derivatives. The discrete Chebychev expansion is used in the r direction, a periodic Fourier expansion in the θ direction (Kessler and Kosloff, 1990). Time integration is performed by the fourth order Runge-Kutta method. The time step is limited by the smallest grid spacing, which is usually in the θ direction. We have found empirically that the time step $dt < 0.4 \cdot (rd\theta)_{\min} / V_{\max}$ where $V_{\max}$ is the highest between the pressure or shear velocity present in the grid ensures stability.

BOUNDARY CONDITIONS

Three different types of boundary conditions are applied at the boundaries of the numerical grid. A free surface or rigid boundary condition is applied at $r = a$, while an absorbing boundary condition is applied at $r = b$ (Figure 1). In a typical calculation, the right hand side of (3) is calculated for the vector $[\dot{U}_r, \dot{U}_\theta, \sigma_{rr}, \sigma_{r\theta}, \sigma_{\theta\theta}]^T$ over the whole grid, and then the values of the results are corrected at the boundaries. This is achieved by setting the correct characteristic variables (Gottlieb et al., 1982; Baylis et al., 1986; Kosloff et al., 1990; Kessler and Kosloff, 1990). The five characteristic variables for the elastic wave equation are:

$$(a) \quad \dot{U}_r + \frac{1}{\rho V_p} \sigma_{rr},$$

$$(b) \quad \dot{U}_\theta + \frac{1}{\rho V_s} \sigma_{r\theta},$$

$$(c) \quad \dot{U}_r - \frac{1}{\rho V_p} \sigma_{rr},$$

$$(d) \quad \dot{U}_\theta - \frac{1}{\rho V_s} \sigma_{r\theta},$$

and

$$(e) \quad \frac{\lambda}{\lambda + 2\mu} \sigma_{rr} - \sigma_{\theta\theta}, \tag{5}$$

where V_p and V_s are pressure- and shear-wave velocities respectively.

The first two variables [(a) and (b)] represent motion propagating inwards, towards decreasing r with velocities V_p and V_s, respectively. The third and fourth variables [(c) and (d)] represent motion propagating outwards, again with velocities V_p and V_s, and the fifth term (e) represents one-dimensional strain compatibility.

At $r = a$ a free-surface boundary condition is applied by keeping the ingoing characteristic variables unchanged and zeroing σ_{rr} and $\sigma_{r\theta}$. This yields the five relations

$$(a) \quad \dot{U}_r^{\text{new}} = \dot{U}_r^{\text{old}} + \frac{1}{\rho V_p} \sigma_{rr}^{\text{old}},$$

$$(b) \quad \dot{U}_\theta^{\text{new}} = \dot{U}_\theta^{\text{old}} + \frac{1}{\rho V_s} \sigma_{r\theta}^{\text{old}},$$

$$(c) \quad \sigma_{\theta\theta}^{\text{new}} = \sigma_{\theta\theta}^{\text{old}} - \frac{\lambda}{\lambda + 2\mu} \sigma_{rr}^{\text{old}},$$

$$(d) \quad \sigma_{rr}^{\text{new}} = 0,$$

and

$$(e) \quad \sigma_{r\theta}^{\text{new}} = 0, \tag{6}$$

where *old* and *new* denote, respectively, values of variables before and after application of the boundary condition.

At $r = b$ the absorbing boundary condition is defined by keeping the characteristic variable describing motion propagating outwards unchanged and setting to zero the characteristic variable describing motion into the grid. The resulting relations are:

$$(a) \quad \sigma_{r\theta}^{\text{new}} = \frac{1}{2}\left[\sigma_{r\theta}^{\text{old}} - \rho V_s \dot{U}_\theta^{\text{old}}\right],$$

$$(b) \quad \dot{U}_\theta^{\text{new}} = \frac{1}{2}\left[\dot{U}_\theta^{\text{old}} - \frac{1}{\rho V_s} \sigma_{r\theta}^{\text{old}}\right],$$

$$(c) \quad \sigma_{rr}^{\text{new}} = \frac{1}{2}\left[\sigma_{rr}^{\text{old}} - \rho V_p \dot{U}_r^{\text{old}}\right],$$

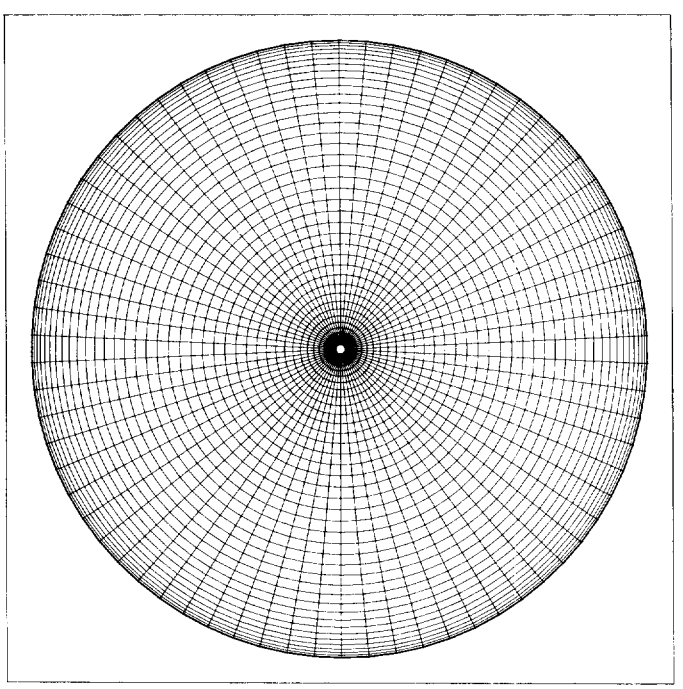

FIG. 2. Chebychev-Fourier two-dimensional polar numerical grid.

$$(d) \qquad \dot{U}_r^{\text{new}} = \frac{1}{2}\left[\dot{U}_r^{\text{old}} - \frac{1}{\rho V_p}\,\sigma_{rr}^{\text{old}}\right],$$

and

$$(e) \qquad \sigma_{\theta\theta}^{\text{new}} = \sigma_{\theta\theta}^{\text{old}} + \left[\sigma_{rr}^{\text{new}} - \sigma_{rr}^{\text{old}}\right]\frac{\lambda}{\lambda + 2\mu}. \qquad (7)$$

SOLUTION IN A MULTIGRID DOMAIN

The system (3) contains four parts which are: operation in the radial direction, operation in the angular direction, source terms, and added terms. Stabilization is based on one-dimensional considerations in the radial direction. The third term of equation (3) includes divisions by r. When $r = b$ is very large compared to $r = a$ the system becomes unstable. This instability exists when $b/a > 80$. In order to keep the algorithm stable we adopted a multigrid approach. We construct a numerical grid such that the numerical algorithm is stable, and then add another grid at its edge, at $r = b$ (Figure 3). In each grid we keep the ratio between the distance of the last and the first grid points smaller than 80, and thus the algorithm is stable in each part of the grid.

The combination of the two grids at their common boundary is implemented by using the characteristic variables of the wave equation. For the absorbing boundary condition the characteristic variables that describe energy that propagates outwards are kept unmodified. For the combination point, the characteristic variable that describes energy that propagates inward and outward are kept unmodified. The values of $[\dot{U}_r, \dot{U}_\theta, \sigma_{rr}, \sigma_{r\theta}, \sigma_{\theta\theta}]^T$ at the nodes common to the two meshes are:

$$(a) \quad \dot{U}_\theta^{\text{new}} = \frac{1}{2}\left[(\dot{U}_\theta^{\text{old}(1)} + \dot{U}_\theta^{\text{old}(2)}) + \frac{1}{\rho V_s}\,(\sigma_{r\theta}^{\text{old}(2)} - \sigma_{r\theta}^{\text{old}(1)})\right],$$

$$(b) \quad \sigma_{r\theta}^{\text{new}} = \frac{1}{2}\left[\rho V_s\,(\dot{U}_\theta^{\text{old}(2)} - \dot{U}_\theta^{\text{old}(1)}) + (\sigma_{r\theta}^{\text{old}(1)} + \sigma_{r\theta}^{\text{old}(2)})\right],$$

$$(c) \quad \dot{U}_r^{\text{new}} = \frac{1}{2}\left[(\dot{U}_r^{\text{old}(1)} + \dot{U}_r^{\text{old}(2)}) + \frac{1}{\rho V_p}\,(\sigma_{rr}^{\text{old}(2)} - \sigma_{rr}^{\text{old}(1)})\right],$$

$$(d) \quad \sigma_{rr}^{\text{new}} = \frac{1}{2}\left[\rho V_p\,(\dot{U}_r^{\text{old}(2)} - \dot{U}_r^{\text{old}(1)}) + (\sigma_{rr}^{\text{old}(1)} + \sigma_{rr}^{\text{old}(2)})\right],$$

and

$$(e) \quad \begin{cases} \sigma_{\theta\theta}^{\text{new}(1)} = \dfrac{\lambda}{\lambda + 2\mu}\,(\sigma_{rr}^{\text{new}} - \sigma_{rr}^{\text{old}(1)}) + \sigma_{\theta\theta}^{\text{old}(1)}, \\ \sigma_{\theta\theta}^{\text{new}(2)} = \dfrac{\lambda}{\lambda + 2\mu}\,(\sigma_{rr}^{\text{new}} - \sigma_{rr}^{\text{old}(2)}) + \sigma_{\theta\theta}^{\text{old}(2)}, \end{cases} \qquad (8)$$

where *new* is the value of the variable after the application of the boundary condition, and *old*(1) and *old*(2) are the values of the variable at the common point of the first and second grid, respectively, before the application of the boundary condition. This correction and the boundary conditions are applied at each time step. $r = b$ (Figure 3) is the combination point for this configuration; absorbing boundary conditions are applied at $r = c$.

Combining numerical grids enables us to use our numerical method for any grid configuration. We can make a to be so small that it would be "unseen" by the wave fronts [see example in Kessler and Kosloff (1990)] and at the same time we can enlarge c to be as big as we need.

The time step for the numerical algorithm is chosen according to the smallest grid spacing in the numerical mesh. A numerical scheme that is based on a cylindrical coordinate system is usually very expensive (in computation time) since the grid spacing in the angular direction is very small, and usually much smaller than the grid spacing in the radial direction. Combining grids can reduce the number of angular points in the interior grid (which covers a small physical space), to increase the angular grid spacing and thus, to increase the time step. Figure 4 shows a typical numerical grid constructed by two smaller grids. The interior part contains 125 angular direction nodes and the exterior part contains 225 angular direction nodes. The number of grid points in the radial direction is 45 in the interior part and 125 in the exterior part. To match the boundary condition at the common grid points it is necessary to have the same number of grid points on each side. This is achieved by interpolating the values of one grid to the same number of points as the second one; after interpolation and applications of the

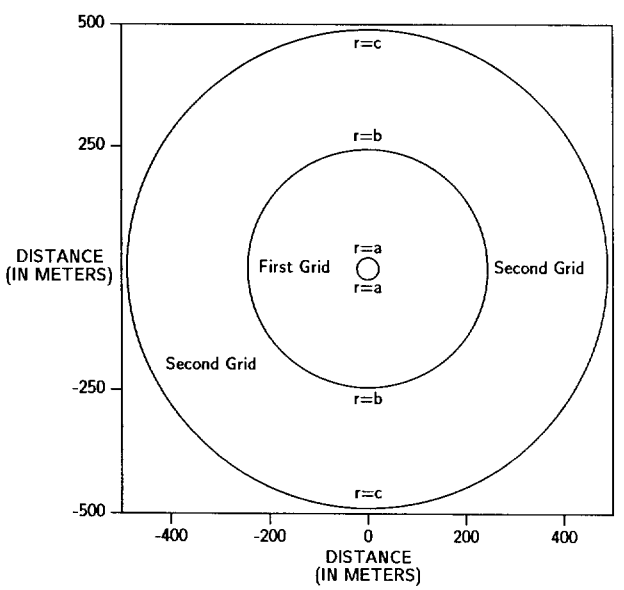

FIG. 3. Combination of two numerical grids (multidomain approach).

boundary conditions [equation (8)], a backward interpolation provides the variables at the original points. Forward and backward interpolations are performed using FFT's.

EXAMPLE: PROPAGATION IN A HOMOGENEOUS MEDIUM

In order to ensure the validity of this method, we compare the numerical result with an analytical result. Figure 5 shows the configuration of this example. The source is a radial direction force at a distance of 163 m from the origin of the grid. Three receivers are considered; A is 222 m to the left of the origin of the grid, B is 358 m below the source and C is at the common grid point, 84 m to the right of the origin of the grid. The pressure-wave velocity in this example is 2000 m/s and the shear-wave velocity is 1300 m/s. Figures 6a and 6b show the radial velocity and the angular velocity snapshots at six times. Figure 7 shows the time history seismograms that were recorded by receivers A, B, and C. The numerical results are plotted by the continuous lines. The analytical results, computed by the two-dimensional elastodynamic Green function (Aki and Richards, 1981) are plotted by dots. In all seismograms the first arrival is the pressure wave and the second is the shear wave.

EXAMPLE: PROPAGATION IN A REGION CONTAINING FLUIDS AND SOLIDS

In a two-part numerical grid, different materials can be specified in each part. For example, a borehole filled with a liquid material can be placed with solid rock. In constructing the numerical grid for this type of experiment, the interior part of the grid propagates acoustic waves only (by setting the shear velocity to zero), and the exterior part of the grid propagates elastic waves. At the liquid-solid interface, we use the characteristic variables of the wave equation.

$\dot{U}_r$ and σ_{rr} are kept continuous by keeping unmodified the characteristic variables $\dot{U}_r + 1/\rho V_p \sigma_{rr}$ and $\dot{U}_r - 1/\rho V_p \sigma_{rr}$, which, respectively, describe motion radially toward and away from the origin of the grid with a velocity V_p; $\sigma_{\theta\theta}$ is found by the characteristic variable $[\lambda/\lambda + 2\mu]\sigma_{rr} - \sigma_{\theta\theta}$ in the solid part, and $\sigma_{\theta\theta} = \sigma_{rr}$ in the liquid part; finally, $\dot{U}_\theta$ is defined in the solid part using the characteristic variable $\dot{U}_\theta + 1/\rho Vs\ \sigma_{r\theta}$, where $\sigma_{r\theta} = 0$.

The following example demonstrates the ability to propagate waves in a solid medium that contains a cylindrical liquid cavity. The source is a radial direction force with peak frequency of 120 Hz at a distance of 163 m from the origin of the grid (Figure 8). The same three receivers as in the previous example are considered. C is located exactly on the liquid-solid interface. The velocity of the pressure wave in the solid part is 2000 m/s, the shear-wave velocity is 1300 m/s, and the velocity of the pressure wave in the liquid is

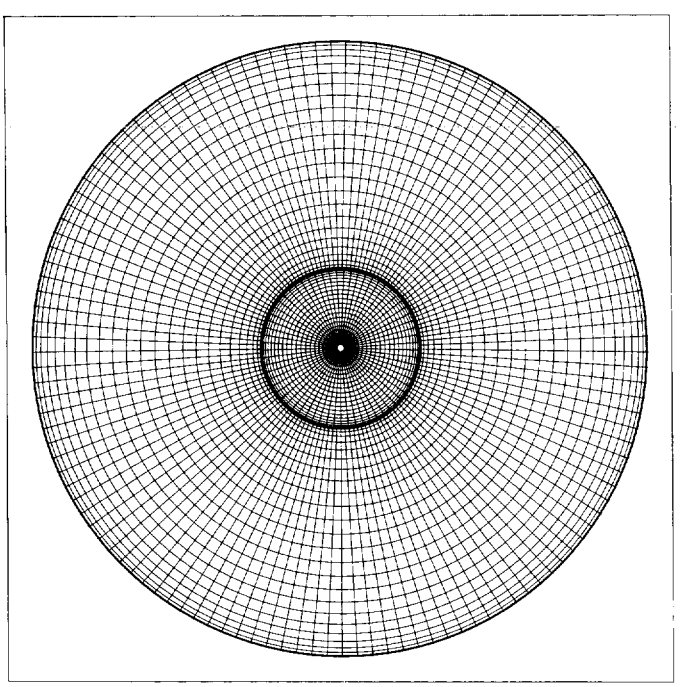

FIG. 4. A numerical grid composed of two parts, each one with different number of nodes in the angular direction.

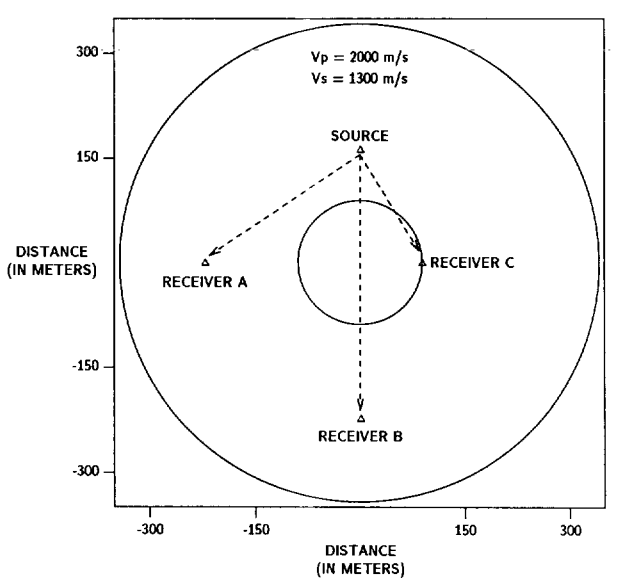

FIG. 5. Configuration of the problem. The numerical grid is composed of two parts. Receiver C is located at the interface between the two grids.

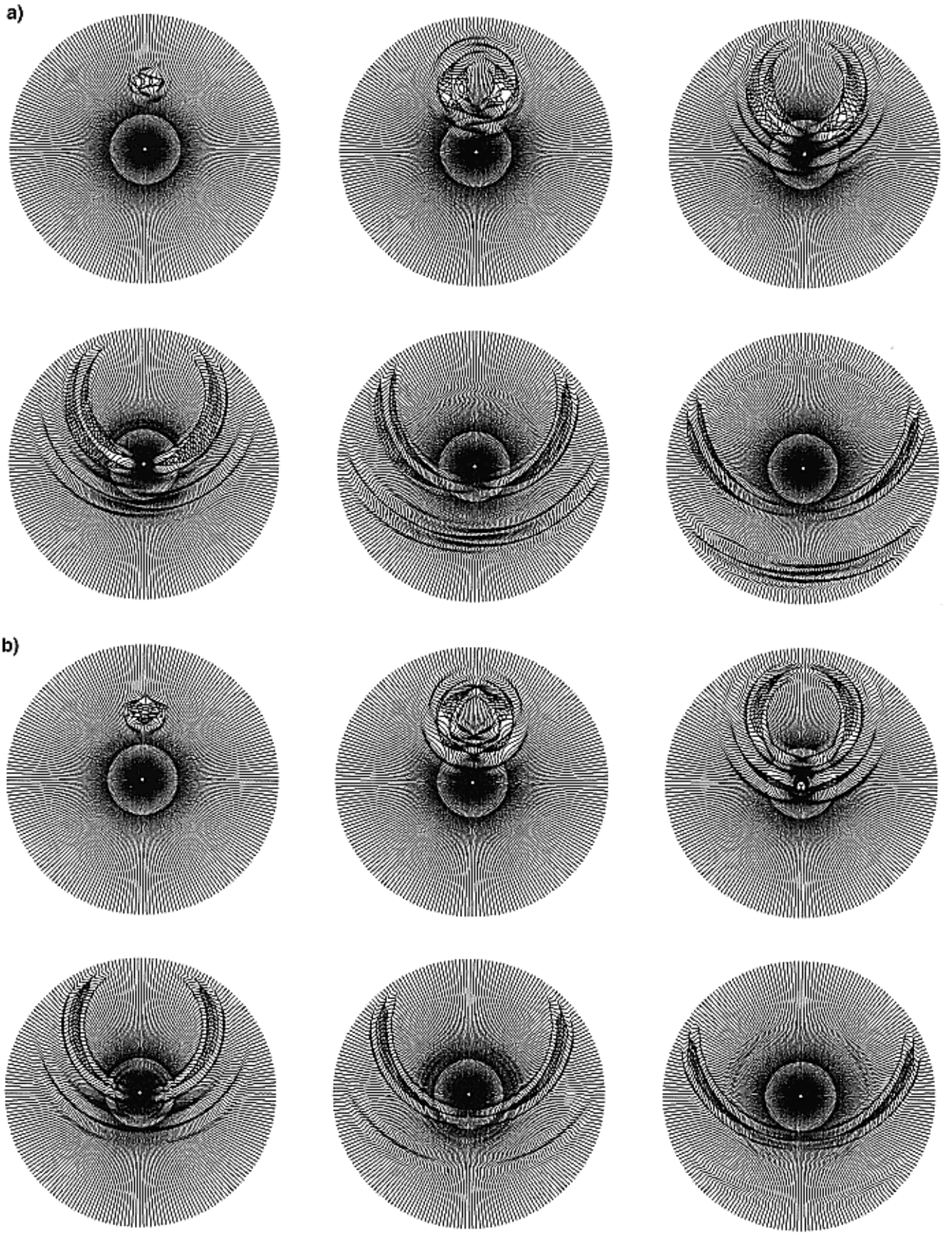

FIG. 6. Wave propagation snapshots in a homogeneous medium. (*a*) Radial velocity field at times 0.06, 0.08, 0.12, 0.16, 0.2, and 0.24 s. (*b*) Angular velocity field at times 0.06, 0.08, 0.12, 0.16, 0.2, and 0.24 s.

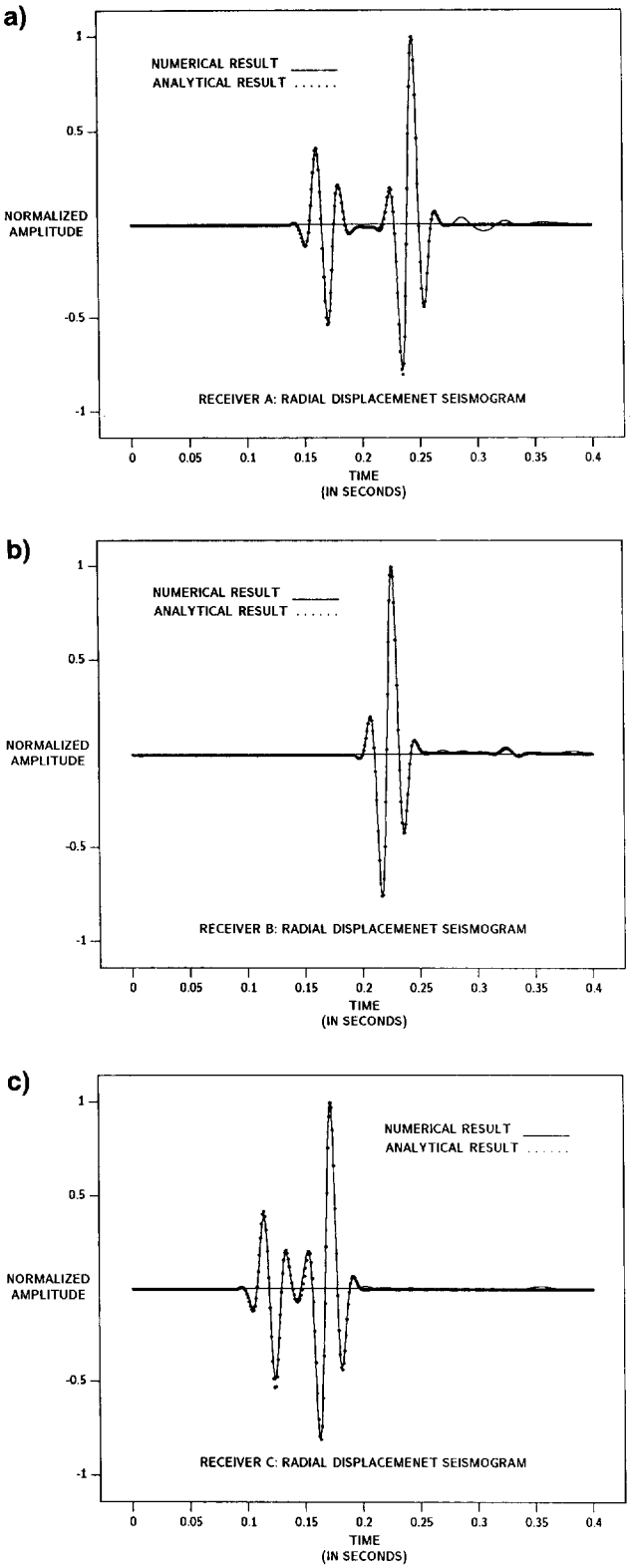

FIG. 7. Seismograms recorded in a homogeneous medium at the receivers in Figure 5. (*a*) Receiver A. (*b*) Receiver B. (*c*) Receiver C.

1500 m/s. Figure 9 shows the radial and the angular velocity snapshots at six times. The pressure and shear waves are visible; the pressure wave travels faster in a solid than in a liquid. At the liquid cylindrical cavity, the shear wave is converted to *P* and then back to *S*. The two wavefronts that pass through the liquid zone are therefore, PP followed by SP converted waves. At later times, we can identify at the liquid-solid interface the surface waves which are called Scholte waves. Figure 10 shows radial particle velocity seismograms recorded by the three receivers. At receivers A and B the pressure arrival and the shear arrival are visible. Receiver B is located exactly below the source, thus the shear component on the seismogram recorded by this receiver is very weak. At receiver C, which is located at the boundary, pressure and shear arrivals are followed by the Scholte surface waves.

To determine the velocity of these surface waves a series of receivers are placed along a radial line at an azimuthal angle of zero degrees (Figure 8). Figure 11 shows three radial particle velocity snapshots at three later times. At these three snapshots the surface waves propagate along the liquid-solid cylindrical interface. Figure 12 shows the time section that was recorded by the radial line of receivers. Four events are marked on the time section. Event A is the pressure wavefront and event B is the shear wavefront. Event C is the first surface wave, arriving at time 0.47 s and event D is the second surface wave, arriving at time 0.72 s. The time difference between events C and D is the time that it takes the surface wave to travel along half of the circumference of the liquid cavity. The radius of this cavity is 84 m

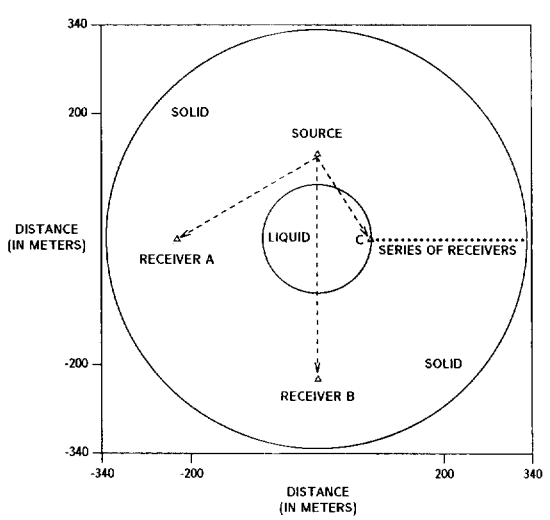

FIG. 8. Configuration of the problem. Liquid cylindrical cavity surrounded by an elastic medium.

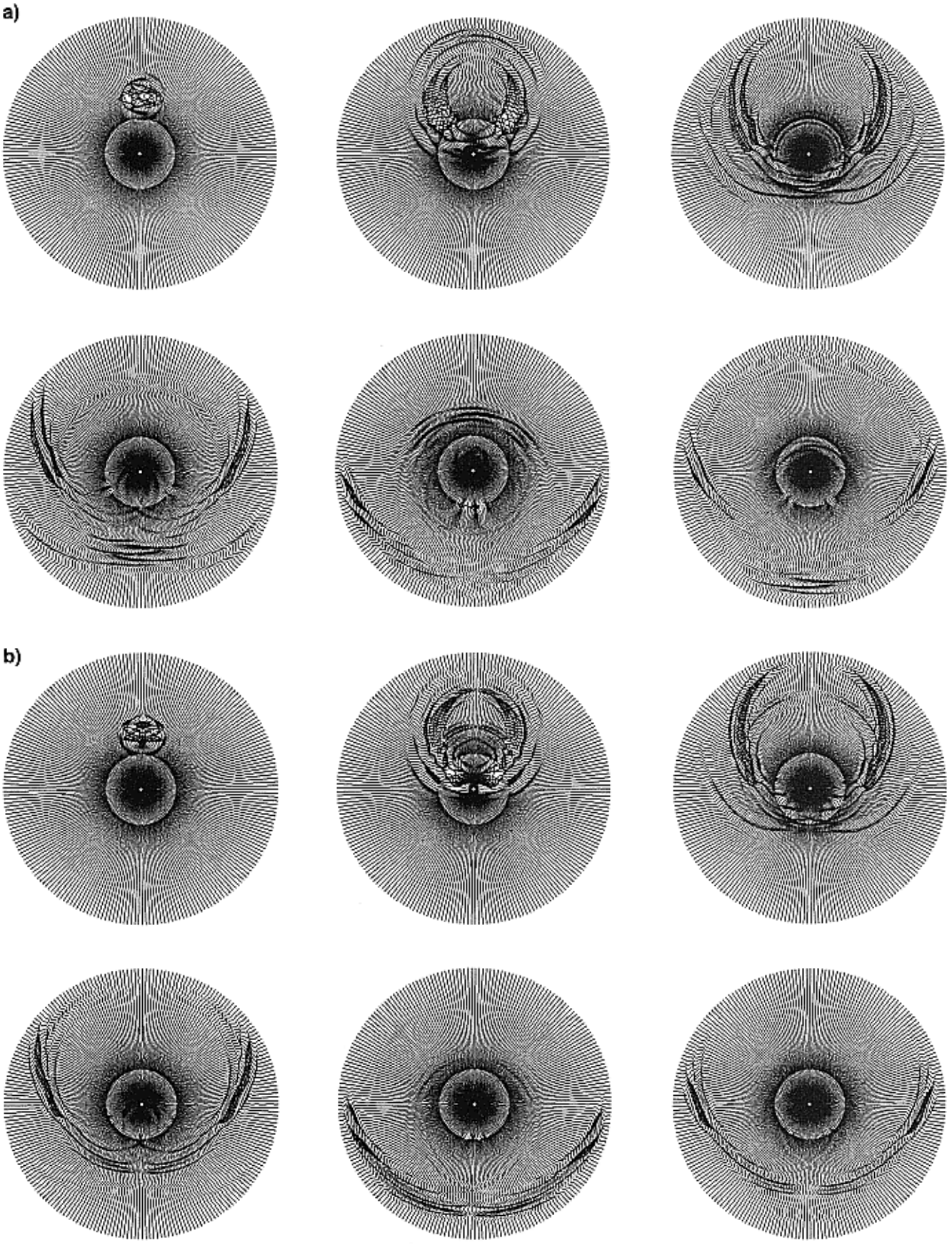

FIG. 9. Wave propagation in a liquid-solid medium. (*a*) Radial velocity field at times 0.04, 0.1, 0.16, 0.22, 0.26, and 0.3 s. (*b*) Angular velocity field at times 0.04, 0.1, 0.16, 0.22, 0.26, and 0.3 s.

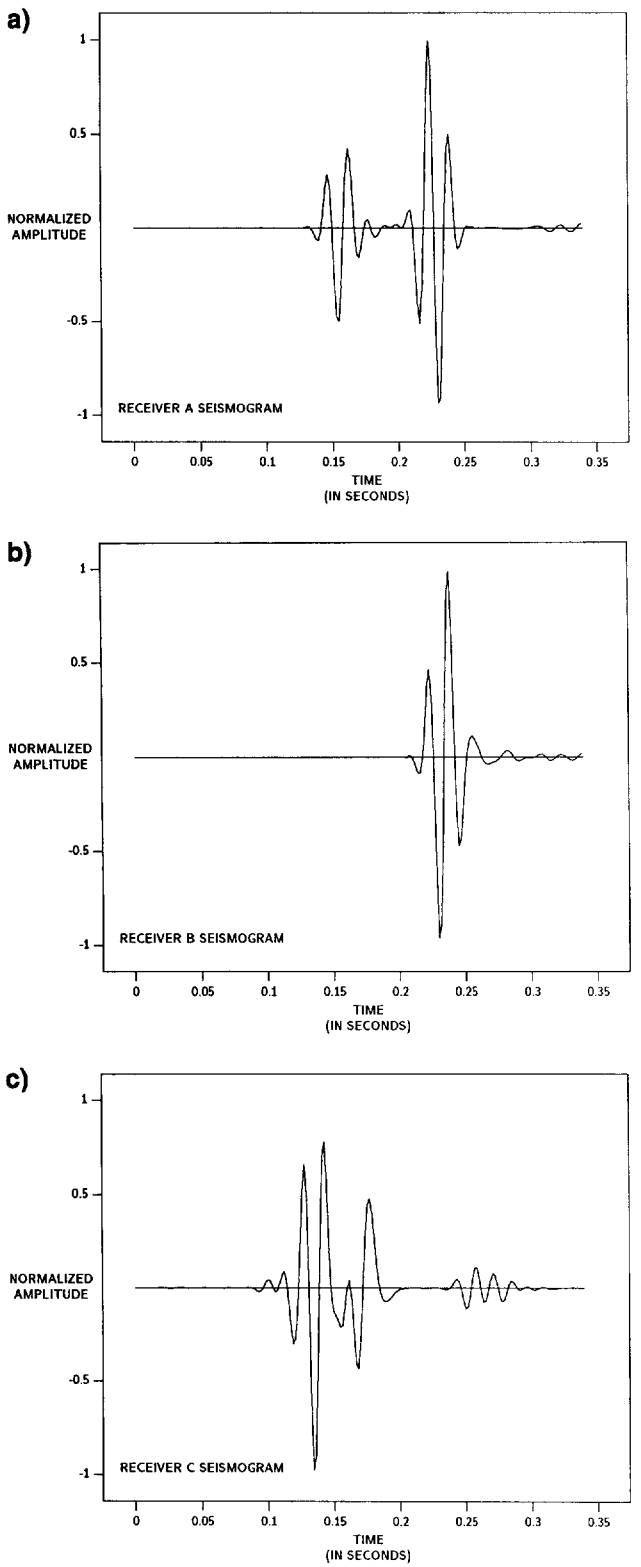

FIG. 10. Seismograms recorded at receivers in Figure 8. (*a*) Receiver A. (*b*) Receiver B. (*c*) Receiver C.

and thus its half circumference is 263 m. The surface waves speed in this example is therefore 974 m/s.

COST CONSIDERATIONS

About two times more grid points are needed in the angular direction than in the radial direction in order to have approximately square grid cells in the middle area of the grid with cylindrical coordinates. Also, at the origin of the grid, the angular grid spacing is about 10 times smaller than the radial direction grid spacing (using a Chebychev expansion in the radial direction). The very small grid spacing in the angular direction results in a very small time step. For a typical configuration, the time step might be 100 times smaller than this in a Cartesian configuration. A great improvement is achieved by using the multigrid approach. We can use very few grid points in the interior grid that covers a small space, and since the smallest grid size is located there we can increase the time step by a factor of three to ten, compared to the same correspondingly single grid configuration. The time step can also be increased by using a coordinate transformation (Kosloff et al., 1990). The Chebychev points $x(i) = \cos(i\pi/N)$, $i = 0, \ldots, N$ are very dense at the boundaries. Using a coordinate stretching, we can define a different set of sampling points that is wider at the edges of the grid (Kosloff and Tal-Ezer, 1992). Using the above coordinate stretching we can improve the cost of the numerical algorithm by a factor of two to ten.

Using Chebychev sampling points requires use of smaller time steps than used with Cartesian coordinate system. If we wish to locate a small cylindrical cavity in the origin of the grid, we will use a time step increment that is about 10 times smaller than used with Cartesian coordinate system. For problems that include a bigger cylindrical body, the time step can be enlarged to be of the same order as that used in Cartesian coordinate system.

CONCLUSIONS

We have presented a new spectral algorithm for elastic wave propagation in 2-D cylindrical coordinates. The method is based on a multigrid approach where each subdomain can have a different number of grid points. Having more than one grid enables reduction of the number of grid points in the interior grid and thus to significantly increase the time step. In each subgrid we use the Chebychev expansion in the radial direction. The Chebychev points are very dense at the boundaries which facilitates application of the boundary conditions as well as the combination of the different grids. By using a coordinate transformation, the distance between the spatial points can be enlarged and thus the time step can be bigger. For the geophysical situation, a cylindrical borehole that is filled with liquid can be constructed by using two grids, the interior filled with liquid and the exterior solid. The next extension towards a realistic simulation of a VSP survey will be a 3-D implementation of the method for solution of wave propagation in the vicinity of a cylindrical cavity. With the knowledge with this 2-D method, a full 3-D configuration is feasible.

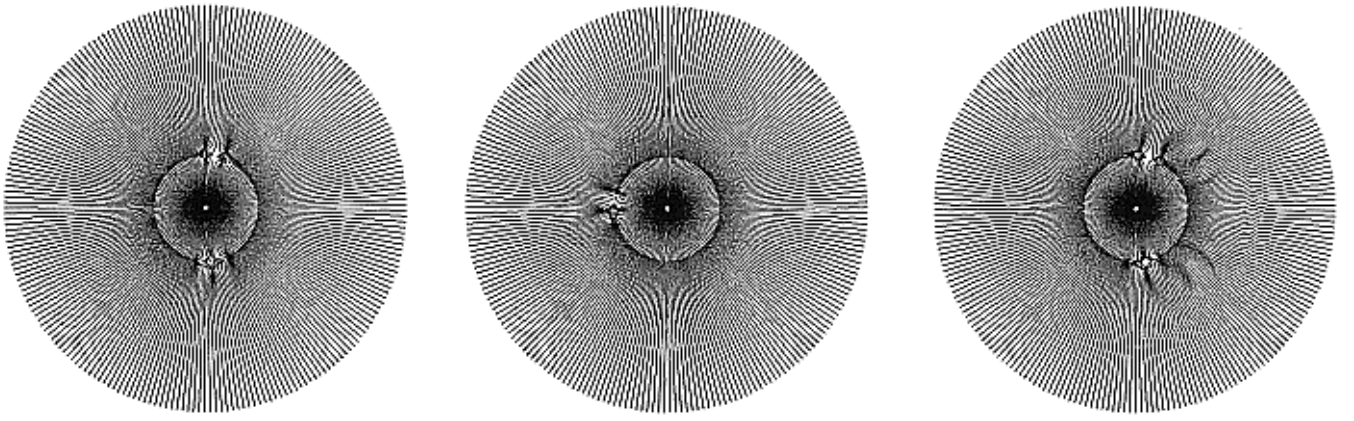

FIG. 11. Wave propagation snapshots at times 0.45, 0.6, and 0.75 s.

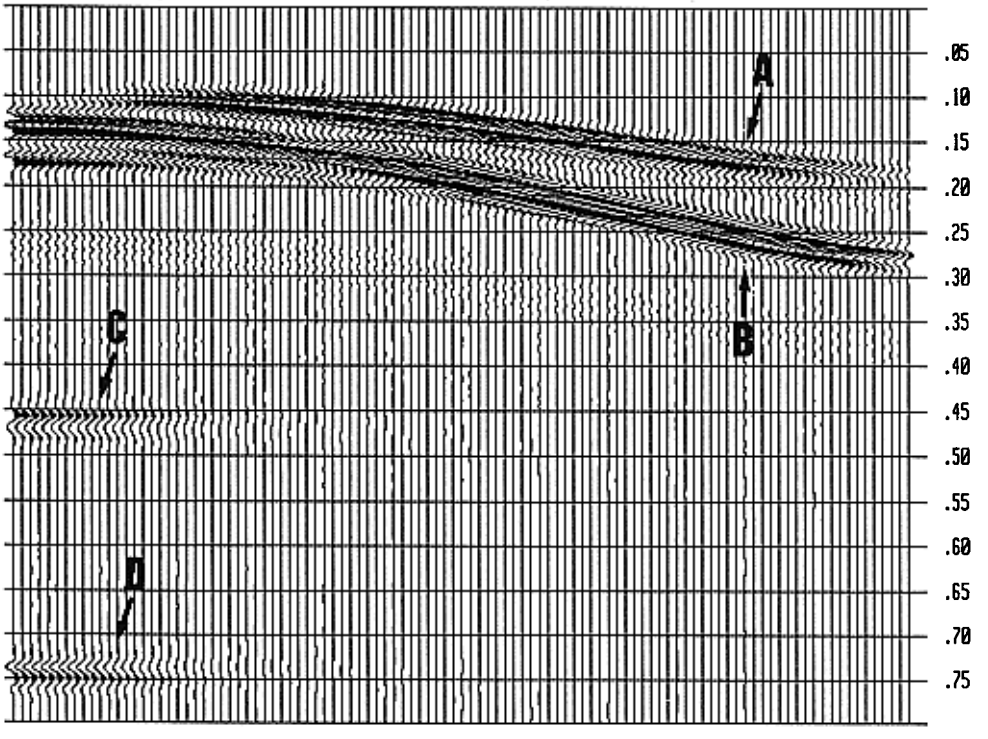

FIG. 12. Time section recorded by the series of receivers shown in Figure 8.

ACKNOWLEDGMENTS

This work was supported by the BMFT project of the Geophysical Institute of Hamburg University and the Commission of the European Communities.

REFERENCES

Aki, K., and Richards, P. G., 1981, Quantative seismology, Theory and methods: W. H. Freeman and Co.

Baylis, A., Jordan, K. E., LeMesurier, B. J., and Turkel, E., 1986, A fourth-order accurate finite-difference scheme for the computation of elastic waves: Bull. Seis. Soc. Am., **76**, 1115–1132.

Fung, Y. C., 1965, Foundations of solid mechanics: Prentice-Hall Inc.

Gottlieb, D., Gunzberger, E. D., and Turkel E., 1982, On numerical boundary treatment for hyperbolic systems: SIAM J. Numer. Anal., **19**, 671–682.

Gottlieb, D., and Orszag, S., 1977, Numerical analysis of spectral methods, Theory and applications: Soc. Ind. Appl. Math.

Hamming, R., 1978, Numerical methods scientists and engineers: McGraw-Hill Book Co.

Kessler, D., and Kosloff, D., 1990, Acoustic wave propagation in 2-D cylindrical coordinates, Geophys. J. Internat., **103**, 577–587.

Kosloff, D., and Baysal, E., 1982, Forward modeling by a Fourier method: Geophysics, **47**, 1402–1412.

Kosloff, D., Kessler, D., Filho, A. Q., Tessmer, E., Behlle, A., and Strahilevits, R., 1990, Solutions of the equations of dynamic elasticity by a Chebychev spectral method: Geophysics, **55**, 734–748.

Kosloff, D., and Tal-Ezer, H., 1992, Modified Chebychev pseudospectral method with $O(N^{-1})$ time step restriction: J. Numer. Phys., submitted.

Tessmer, E., Kessler, D., Kosloff, D., and Alfred, B., 1992, Multidomain Chebychev-Fourier method for the solution of the equations of motion of dynamic elasticity: Comp. Phys., submitted.